Supporting Information

Interfacial engineering of $Cu\text{-}Fe_2O_3$ nanotube arrays with built-in electric-field and oxygen vacancies effects for boosting electrocatalytic reduction of nitrate

Yihong Gao [a,1], Kun Huang [a,1], Chen Yan [a] , Shikuo Li [b,*], Hui Zhang [b,*], Longjiu Cheng [a], Fangzhi Huang [a,*]

Laboratory of Clean Energy & Environmental Catalysis, AnHui Province Key Laboratory of Chemistry for Inorganic/Organic Hybrid Functionalized Materials, School of Chemistry and Chemical Engineering, Anhui University, Hefei 230601, P. R. China; School of Materials Science and Engineering, Anhui University, Hefei 230601, P. R. China

Received (in XXX, XXX) Xth XXXXXXXXX 20XX, Accepted Xth XXXXXXXXX 20XX

DOI: 10.1039/b000000x

Experimental details

Text S1. Ion concentration detection methods.

Colorimetric methods were applied to determine the concentration of nitrate, nitrite and ammonium [1-3]. The ultraviolet-visible (UV-Vis) spectrophotometer was used to detect the ion concentration of pre- and post-test electrolytes after diluting to appropriate concentration to match the range of calibration curves [4-6]. The specific detection methods are as follow:

Determination of nitrate-N:

Nitrate concentrations were measured following standard methods. Firstly, a certain amount of electrolyte was taken out from electrolytic cell and diluted to 5 mL in the detected range. Then 100 μL 5 wt% sulfamic acid solution was added into the aforementioned solution, standing for 10 minutes at room temperature. The absorption spectrum was tested using an ultraviolet-visible spectrophotometer and the absorption intensities at wavelength of 220 nm and 275 nm were recorded. The final absorbance value was calculated by the equation: $A = A_{220nm} - 2A_{275nm}$. The calibration curve was plotted using a series of concentrations from 0 to 2.00 ppm. And the sodium nitrate applied for plotting calibration curve was pretreated by drying in the oven at 105-110 ° C for 2 h in advance.

Determination of nitrite-N:

A mixture of p-aminobenzenesulfonamide (0.4 g), N-(1-Naphthyl) ethylenediamine dihydrochloride (0.02 g), ultrapure water (5 mL) and phosphoric acid (1 mL, ρ=1.70 g/mL) was used as a color reagent. A certain amount of electrolyte was taken out from the electrolytic cell and diluted to 5 mL to detection range. Next, 0.1 mL color reagent was added into the aforementioned 5 mL solution and mixed uniformity, and the absorption intensity at a wavelength of 540 nm was recorded after sitting for 20 min. The concentration-absorbance curve was calibrated using a series of standard sodium nitrite solutions.

Detection of ammonium-N:

The Nessler's reagent was prepared by dissolving 0.35 g KI, 0.5 g HgI_2 in 5 mL 4.0 M NaOH solution successively and then the mixed solution was placed in the dark without disturbance for 24 h, finally the liquid supernatant was transferred into a Teflon bottle refrigerated for use. For colorimetric assay, a certain amount of electrolyte was taken out from electrolytic cell and diluted to 5 mL to detection range. Next, 0.1 mL potassium sodium tartrate solution (ρ = 500 g L^{-1}) was added and mixed thoroughly, then 0.1 mL Nessler's reagent was put into the solution. The absorption intensity at wavelength of 420 nm was recorded after sitting for 20 min. The concentration-absorbance curve was made using a series of standard ammonium chloride solutions from 0 to 2.00 ppm and the ammonium chloride crystal was dried at 105 °C for 2 h in advance.

Text S2. Materials characterization

Morphology of the catalysts were characterized using scanning electron microscopy (SEM, Zeiss Supra 40) and transmission electron microscopy (TEM, JEOL JEM-2010) with an energy-dispersive spectroscopy (EDX) for elemental mapping. X-ray Diffraction (XRD, MAP18AHF) was performed to determine the crystal structure of the samples. The chemistry composition was characterized by X-ray photoelectron spectroscopy (XPS, ESCA Lab MKII). The surface potential images were measured using Kelvin probe force microscopy techniques (AFM5500M, HITACHI) under an ambient atmosphere. By EMX nano electron paramagnetic resonance (EPR) spectrometer, the concentration of OVs were detected. The ultraviolet-visible (UV-Vis) absorbance spectra were measured on Shimadzu UV-3900 spectrophotometer. The isotope labeling experiments were measured by ^1H NMR measurement (JNM-ECZ600R). The reaction intermediate information was studies by In-situ Raman spectroscopy (in Via-Reflex).

Text S3. Electrochemical Nitrate Reduction Experiment.

The electrochemical nitrate reduction reaction experiments were carried out using a standard three-electrode system in a single-chamber electrolytic cell. The catalyst loaded on CF, saturated calomel electrode (SCE), and platinum foil were used as the working electrode, reference electrode, and counter electrode, respectively. 0.5 M Na_2SO_4 solution was used as the electrolyte, and a certain concentration of $NaNO_3$ was added to the electrolytic cell as the target reactant. All the electrochemical measurements were performed using CHI 660E electrochemical workstation (CHI 660E, Chenhua, Shanghai). The potential is recorded under a

standard hydrogen electrode, and the conversion formula is E(RHE)=E(SCE)+0.0591pH+0.2438. Before conducting the nitrate electroreduction test, the linear sweep voltammetry was performed to make the polarization curve reach a steady state. A constant potential test was carried out at different potentials for 2 hours.

Text S4. Pilot-Scale Tests of Electrochemical Nitrate Reduction.

The industrial electrocatalytic nitrate reduction experiment was carried out using a two-electrode system in a pilot-scale reactor. The catalyst loaded on CF and titanium plate were used as the working electrode and counter electrode, respectively. 0.5 M Na_2SO_4 solution was used as the electrolyte, and a certain concentration of $NaNO_3$ was added to the electrolytic cell as the target reactant. The size of the reactor is 77×59×40cm, and it can process 180L of wastewater. In addition, in order to enhance the catalytic efficiency, the catalyst is connected in series into an electrode group. The size of all electrodes is maintained at 20 × 30 cm ◦ A constant potential test was carried out at different potentials for 4 hours.

Text S5. N isotope labeling experiments

The N isotopic labeling experiments were carried out using the aforementioned electrochemical nitrate reduction methods in the electrolyte (50 ppm NO_3^--N) with $Na^{15}NO_3$ and $Na^{14}NO_3$ as N source, respectively. The amount of produced $^{15}NH_4^+$ and $^{14}NH_4^+$ was quantified by the ^{1}H-Nuclear Magnetic Resonance (NMR) spectroscopy. For quantitative, we prepared a series of standard solutions and plotted the standard curve. First, a series of $^{15}NH_4^+$ solutions with known concentration were prepared in 0.5 M Na_2SO_4 as standards; Second, 50 mL of the $^{15}NH_4^+$ and standard solution with different concentration was mixed with 50 ppm maleic acid; Third, 50 μL deuterium oxide (D_2O) was added in 0.5 mL above mixed solution for the NMR detection; Fourth, the calibration was achieved using the peak area ratio between $^{15}NH_4^+$ and maleic acid because the $^{15}NH_4^+$ concentration and the area ratio were positively correlated. Similarly, the amount of $^{14}NH_4^+$ was quantified by this method when $Na^{14}NO_3$ was used as the feeding N-source.

Text S6. In situ Raman characterization

To detect the intermediates of nitrate reduction reaction, a Raman electrochemical cell with Pt wire and an Ag/AgCl electrode were used as the counter and the reference electrodes, respectively, for in situ Raman measurements. Raman spectroscopy was performed on a Laser Micro-Raman spectrometer at room temperature with an Ar^+ laser of 514.5 nm excitation. A proper electrochemical cell was selected to fit the Raman spectrometer to perform the in-situ Raman test. Laser beams focus on the sample through a hole in the middle of the cell to collect Raman information. To study the intermediates on the surface of Cu-Fe_2O_3 nanotubes in the nitrate reduction process, the amperometry i–t curve (i–t) test method was employed to apply different voltages to the electrode. In addition, the spectra were obtained by applying single potential steps of 0.1 V from 0 to -1.0 V *vs.* RHE.

Text S7. Calculation of the conversion, yield, selectivity, and Faradaic efficiency.

The NO_3^- conversion rate was calculated as follows:

$$NO_3^- \text{ conversion} = \Delta C_{NO3-} / C_0 \times 100\% \quad (1)$$

The selectivity of the product can be calculated by:

$$NH_4^+ \text{ selectivity } (S_{NH4+}) = C_{NH4+} / \Delta C_{NO3-} \times 100\% \quad (2)$$

$$NO_2^- \text{ selectivity } (S_{NO2-}) = C_{NO2-} / \Delta C_{NO3-} \times 100\% \quad (3)$$

The yield of NH_4^+(aq) was calculated using equation:

$$\text{Yield } NH_4^+ = (C_{NH4+} \times V) / (M_{NH4+} \times t \times m) \quad (4)$$

The Faradaic efficiency was calculated as follows:

$$\text{Faradaic efficiency} = (8F \times C_{NO3-} \times V) / (M_{NO3-} \times Q) \times 100\% \quad (5)$$

where C_{NH4+} is the concentration of $NH_4^+{}_{(aq)}$, C_{NO2-} is the concentration of $NO_2^-{}_{(aq)}$, ΔC_{NO3-} is the concentration difference of NO_3^- before and after electrolysis, C_0 is the initial concentration of NO_3^-, V is the electrolyte volume, t is the electrolysis time, m

is the mass of catalyst, F is the Faradaic constant (96485 C mol^{-1}), Q is the total charge passing the electrode.

Text S8. Theoretical Simulation

Density functional theory (DFT) calculations were performed as implemented in the plane wave set Vienna ab initio Simulation Package (VASP) code [7]. Generalized gradient approximation (GGA) with the exchange-correlation functional in the Perdew-Burke-Ernzerhof (PBE) form was adopted [8]. DFT + U method was used to better describe the on-site coulomb (U) correlation of the localized 3d electrons for transition metal Cu with U - J = 3.42 eV [9]. Spin polarization was considered for all calculations. The kinetic-energy cut off was set as 500 eV. The convergence threshold of 10^{-4} eV was set for self-consistent field (SCF) iteration between two electronic steps. Conjugate gradient method was adopted for geometry optimization with forces on each atom less than 0.05 eV/Å. A 4 × 4 unit cell of Cu (111) surface with four atomic layers and a 2 × 2 unit cell of Fe_2O_3 (220) surface with four Fe-O bilayers were used to ensure the lager lateral lattice (~1 nm). A vacuum layer of 15 Å was inserted along the z direction to prevent the periodic image interactions. The bottom two Cu atomic layers or Fe-O bilayers were fixed while other layers and the adsorbates were fully relaxed during structural optimizations. A k-point mesh of 3 × 3 × 1 was sampled for the Brillouin zone. Cu-Fe_2O_3 NTs were also modeled by a 3×3 Cu surface by removing two electrons from the system to reflect the interfacial charge transfer. Here, the chemical reaction considered can be summarized with the reaction equations below.

$$* + NO_3^- \rightarrow *NO_3 + e^- \quad (6)$$

$$*NO_3 + 2H^+ + 2e^- \rightarrow *NO_2 + H_2O \quad (7)$$

$$*NO_2 + 2H^+ + 2e^- \rightarrow *NO + H_2O \quad (8)$$

$$*NO + H^+ + e^- \rightarrow *HNO \quad (9)$$

$$*HNO + H^+ + e^- \rightarrow *H_2NO \quad (10)$$

$$*H_2NO + H^+ + e^- \rightarrow *O + NH_3 \quad (11)$$

$$*O + 2H^+ + e^- \rightarrow * + H_2O \quad (12)$$

where * represents the active site. Then, the reaction free energy change can be obtained with the equation below:

$$G = E_{DFT} + E_{ZPE} - TS \quad (13)$$

where E_{DFT} and E_{ZPE} are the total energy and zero-point energy calculated with VASP, TS is the entropy contribution at 298.15 K. Computational hydrogen electrode (CHE) model proposed by Nørskov et al was used to calculate the free energy change of each reaction step that involves an electrochemical proton-electron transfer [10]. In this model, zero voltage is defined based on the reversible hydrogen electrode (RHE), in which the reaction

$$H^+ + e^- \leftrightarrow 1/2\ H_2 \quad (14)$$

is defined to be in equilibrium at zero voltage, at all values of pH, at all temperatures, and with H_2 at 101325 Pa pressure. Therefore, the free energy of a proton-electron pair ($G(H^+ + e^-)$) is equal to half of the free energy of gaseous hydrogen (1/2 GH_2) at a potential of 0 V.

Finite element analysis (FEA): The simulations were carried out using COMSOL Multiphysics 5.6. The "Transport of Diluted Species" and "Electrostatics" modules of COMSOL were adopted in a Stationary mode with Parametric Sweep of the index Surface Charge Density to investigate the influence on the concentration of anions.

Mass transport and electric fields in the numerical model are described by the Poisson-Nernst-Planck (PNP) equation, and the concentration and flow of ions are governed by Nernst-Placnk equation, defined as follows,

$$J_i = -D_i \left(\nabla c_i + \frac{zeF}{RT} c_i \nabla \Phi\right)$$

Where, F is Faraday's constant, R is the gas constant, T (298.15 K) is the absolute temperature, Φ is the electrical potential, D_i, c_i and z_i are the diffusion coefficient, concentration and charge of species i, respectively. The electric field is determined by the Possion equation,

$$\nabla^2 \Phi = \frac{\rho}{\varepsilon 0 \varepsilon R}$$

where ε_0 and ε_R are the permittivity of space and the dielectric constant of the medium, respectively. The space charge density ρ depend on the concentration of charged species in the solution according to,

$$\rho = F\Sigma z_i C_i$$

These equations govern molecular transport and electric field strength in the NEA geometry and were used to obtain the simulation results.

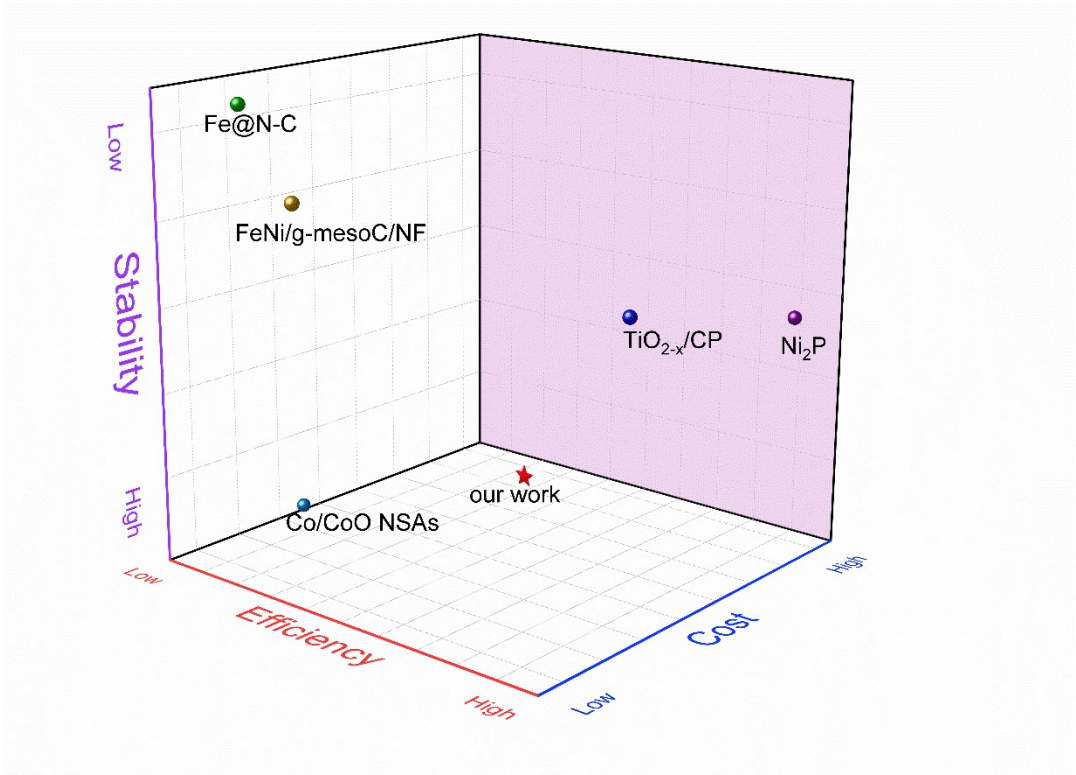

Fig. S1. Performance comparison of various materials.

(a) Cost. The reagents used for preparation of Cu-Fe_2O_3-60 are low-cost and readily available. The cost of the material is only 0.4 ¥/cm^2, which is lower than other reported precious metal materials 11-14. (b) Efficiency. The unique Cu-Fe_2O_3-60 exhibited excellent Faradaic efficiency (80.1%) and selectivity (88.47%) for ENRA. (c) Stability. Compared with other materials, the catalytic stability of Cu-Fe_2O_3-60 remains after several cycles.

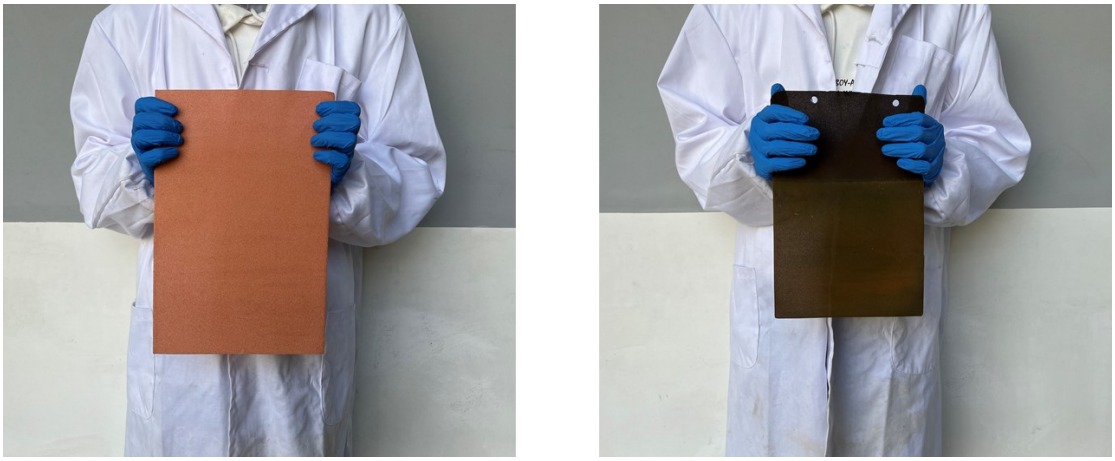

Fig. S2. Photographs of a pristine Cu foam (left) and Cu-Fe_2O_3-60 is loaded on Cu foam (right).

Scalability. The size of the materials can be flexibly controlled, which can not only meet the experimental level, but also be appropriately enlarged to meet the industrial level.

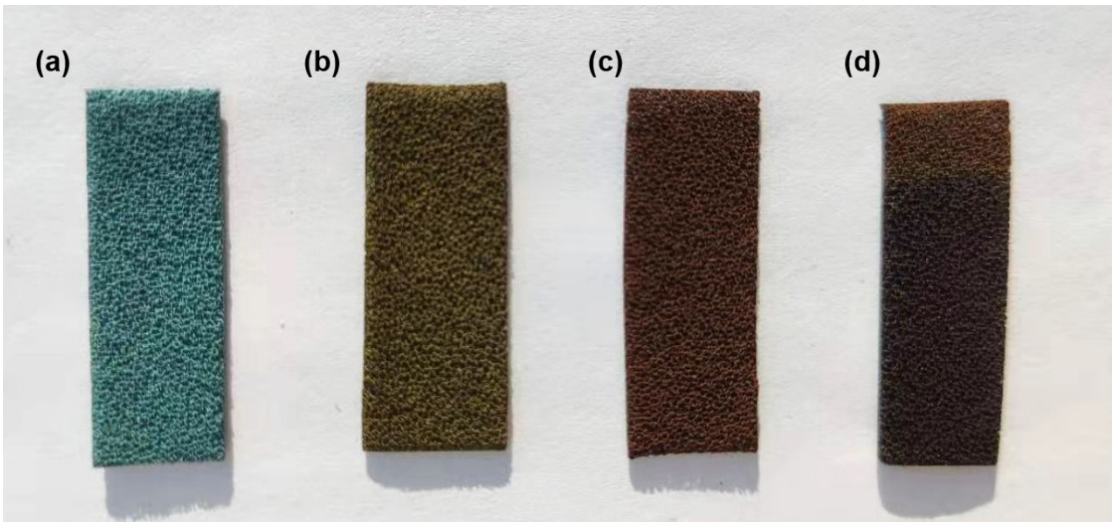

Fig. S3. Optical photographs of as-prepared samples based on CF. (a) $Cu(OH)_2$ NWs, (b) $Cu(OH)_2$-$Fe(OH)_3$ NTs, (c) CuO-Fe_2O_3-60, (d) Cu-Fe_2O_3-60.

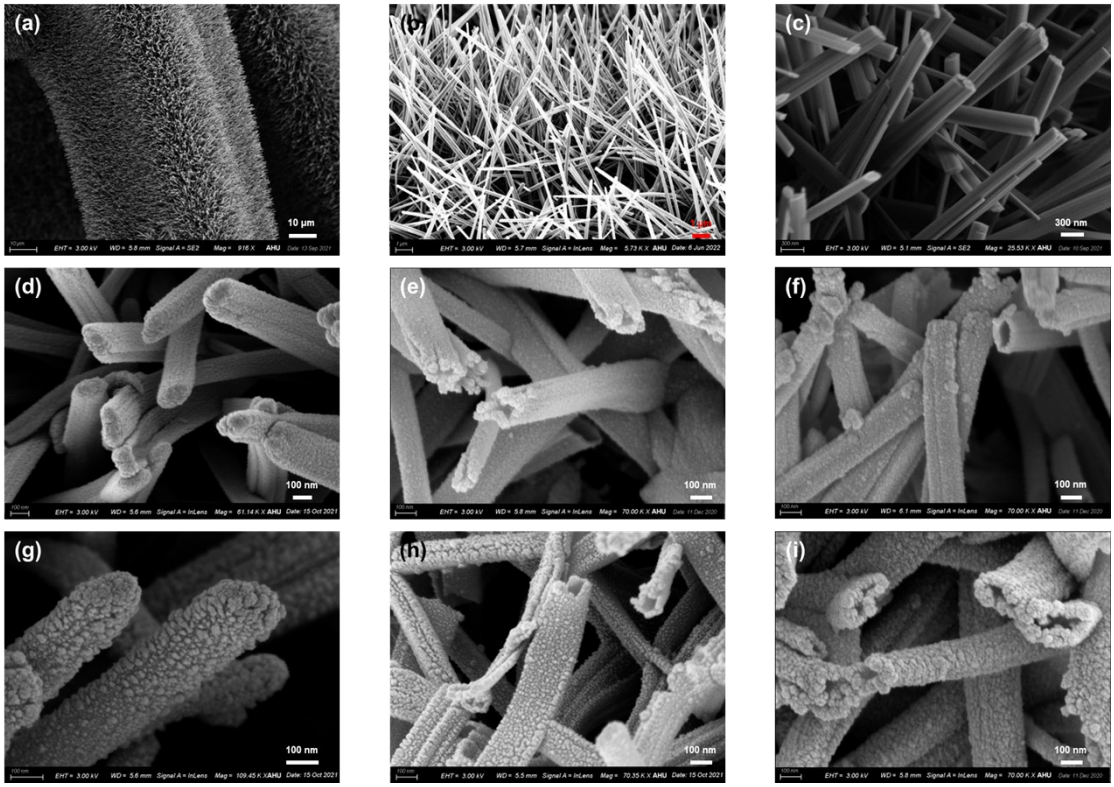

Fig. S4. SEM images of (a-c) $Cu(OH)_2$ NWs, (d) $Cu(OH)_2$-$Fe(OH)_3$-30, (e) $Cu(OH)_2$-$Fe(OH)_3$-60, (f) $Cu(OH)_2$-$Fe(OH)_3$-120, (g) CuO-Fe_2O_3-30, (h) CuO-Fe_2O_3-60, (i) CuO-Fe_2O_3-120.

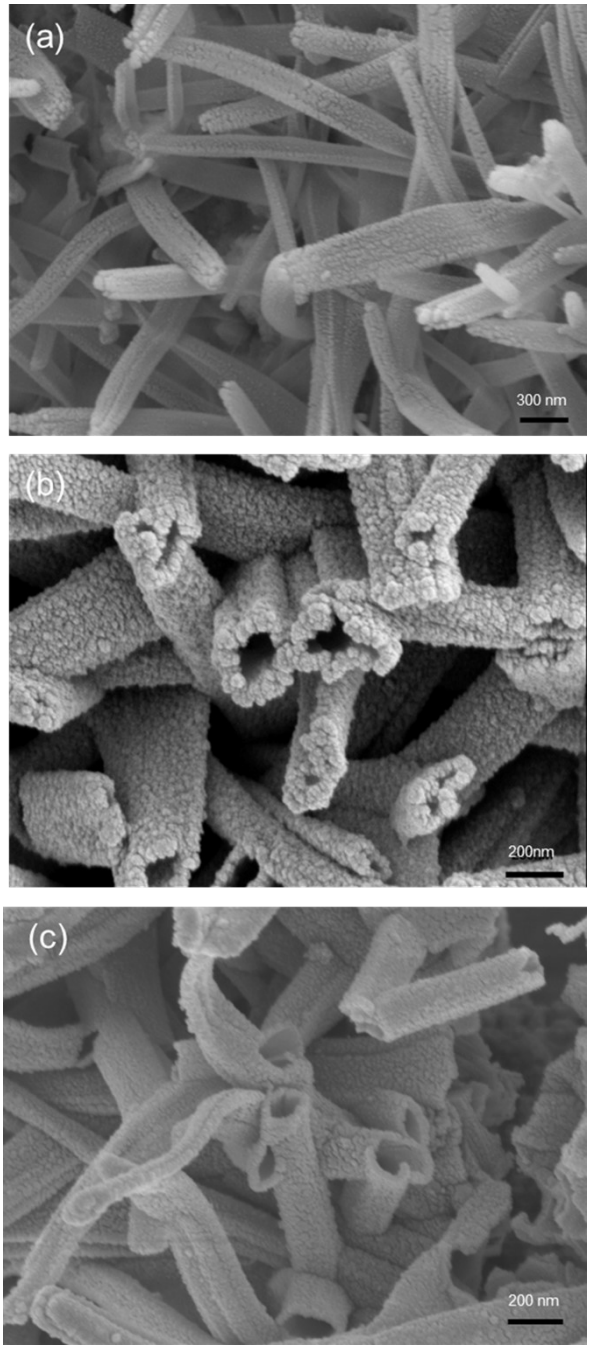

Fig. S5. SEM images of (a) Cu-Fe_2O_3-30, (b) Cu-Fe_2O_3-60, (C) Cu-Fe_2O_3-120.

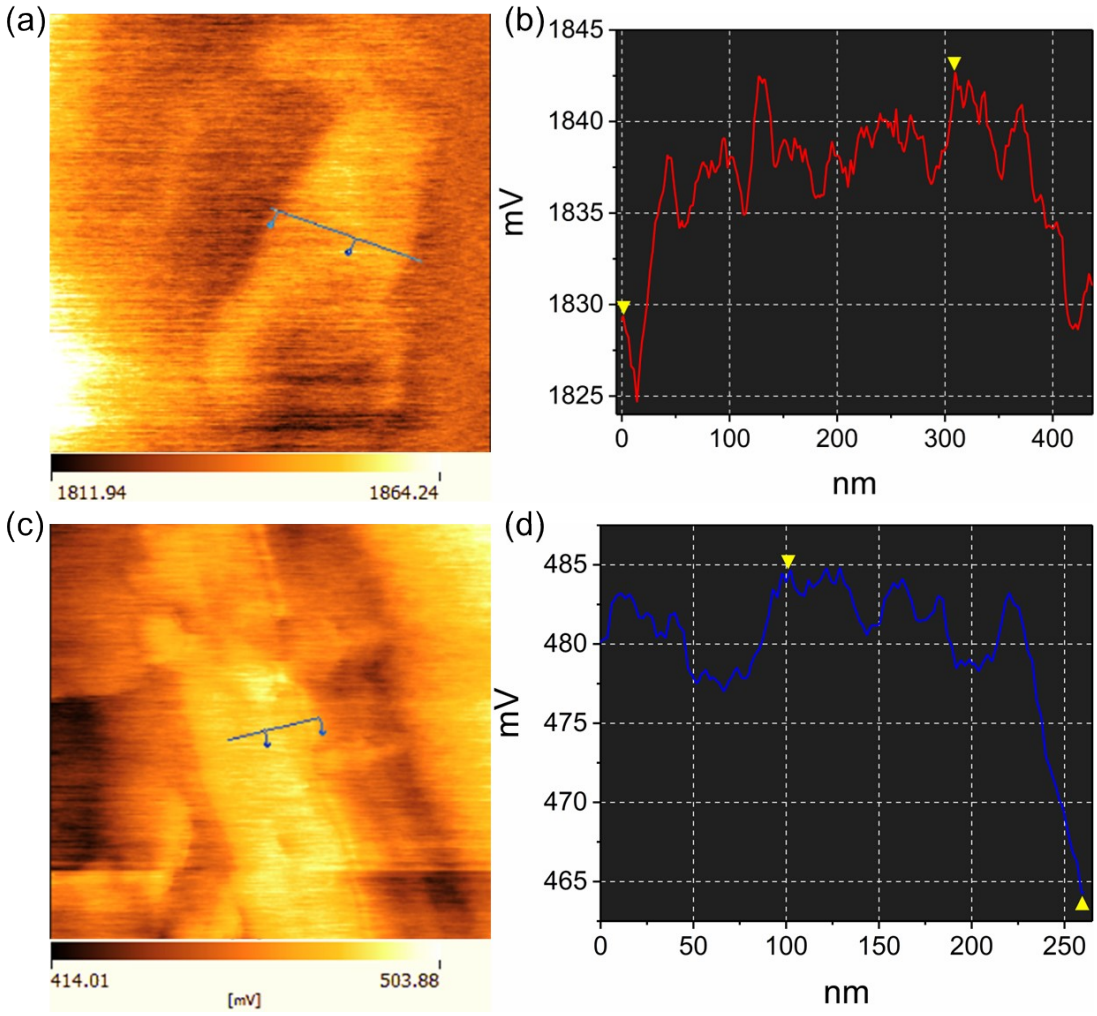

Fig. S6. Built-in electric field distribution of (a) Cu-Fe_2O_3-30, and (c) Cu-Fe_2O_3-120. (b, d) Surface potential values extracted across the lines in a, c.

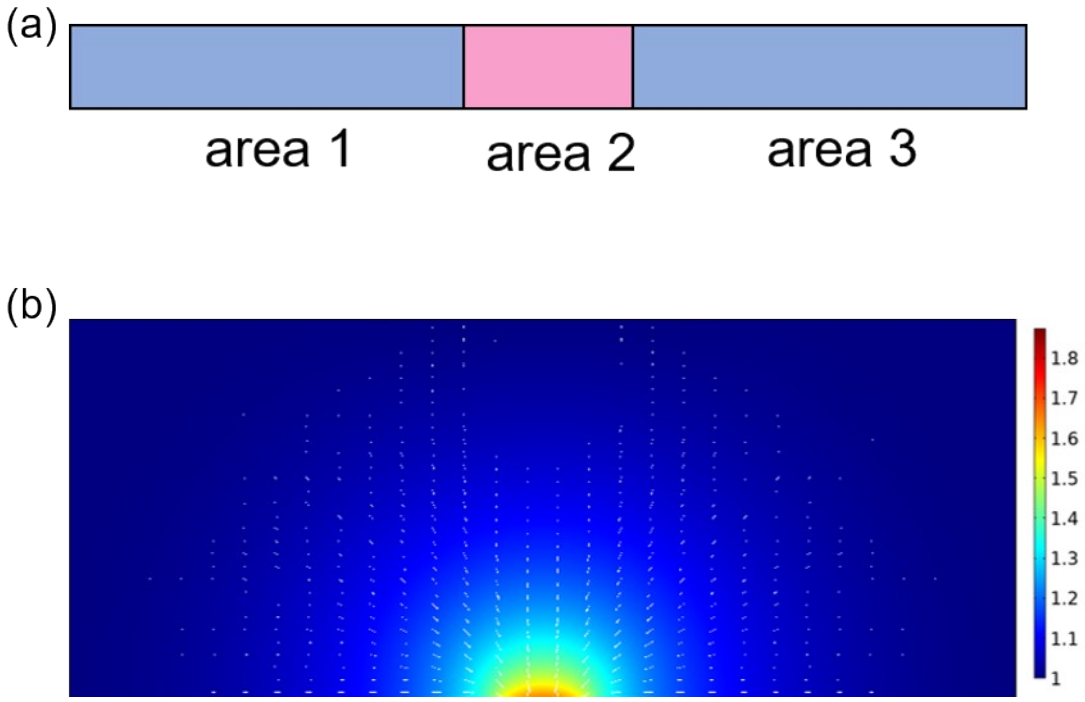

Fig. S7. (a) The model of the Cu-Fe_2O_3 NTs electrode surface using a two-dimension plane for finite element numerical calculation, the area 2 (30 nm × 10 nm) represents Cu nanoparticles, the area 1 and 3 (100 nm × 10 nm) represent Fe_2O_3 nanoparticles. (b) The NO_3^- anions distribution on the surface of electrode by introducing a slight amount of positive charges (0.05 C/m^2) in area 2.

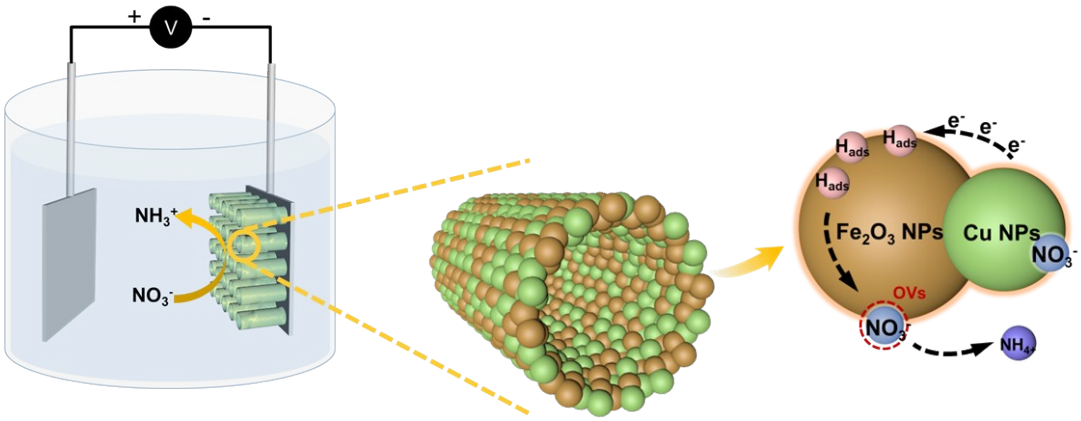

Fig. S8. Application of Cu-Fe_2O_3-60 in electrochemical nitrate reduction.

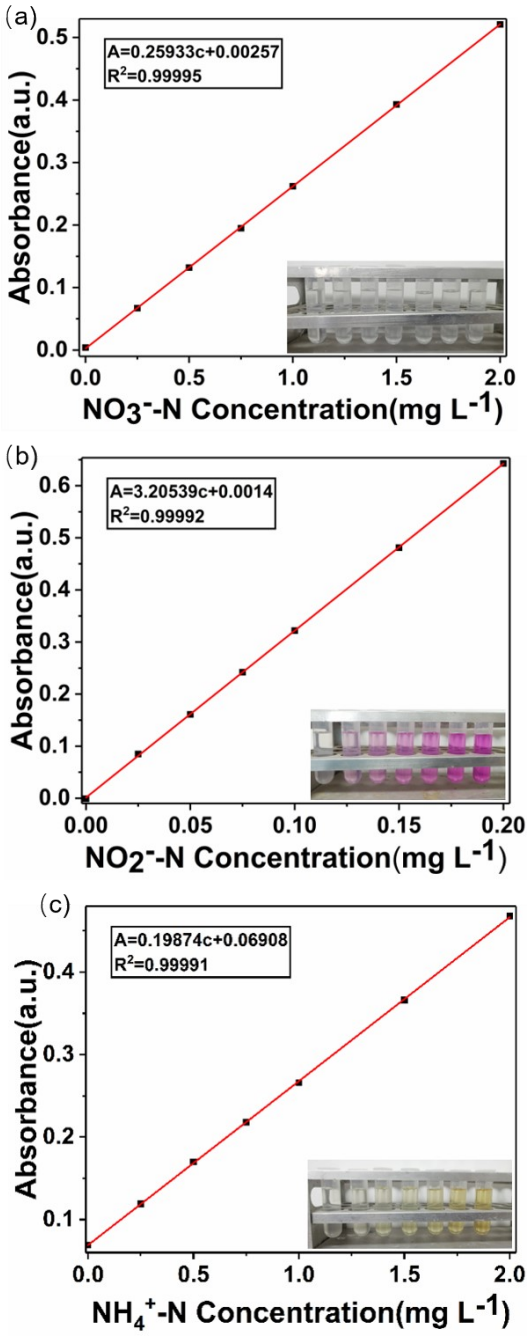

Fig. S9. The UV-Vis absorption spectra and the corresponding calibration curves. (a) NO_3^--N, (b) NO_2^--N, (c) NH_4^+-N, and the inset in (c) is the photograph of chromogenic results.

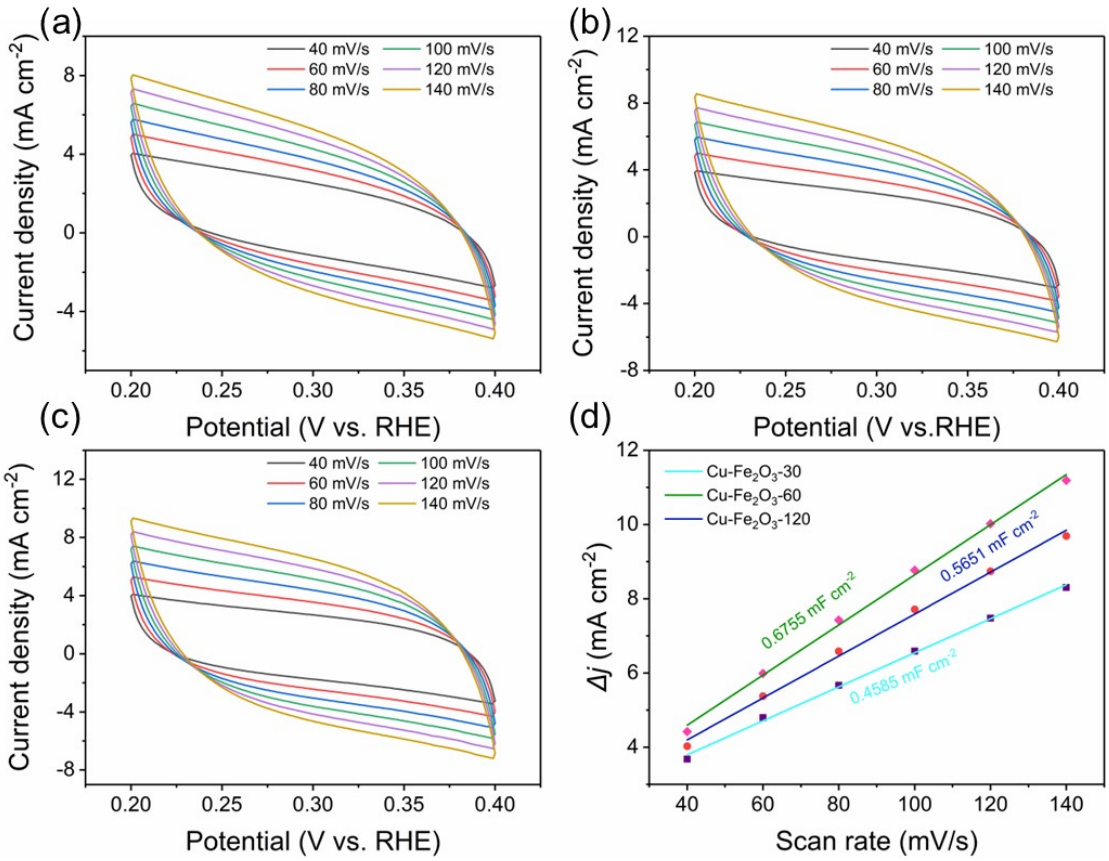

Fig S10. Cyclic voltammetry curves of the samples at different scan rates. (a)Cu-Fe_2O_3-30; (b) Cu-Fe_2O_3-60; (c) Cu-Fe_2O_3-120. (d) f) C_{dl} values of Cu-Fe_2O_3-30 Cu-Fe_2O_3-60 and Cu-Fe_2O_3-120

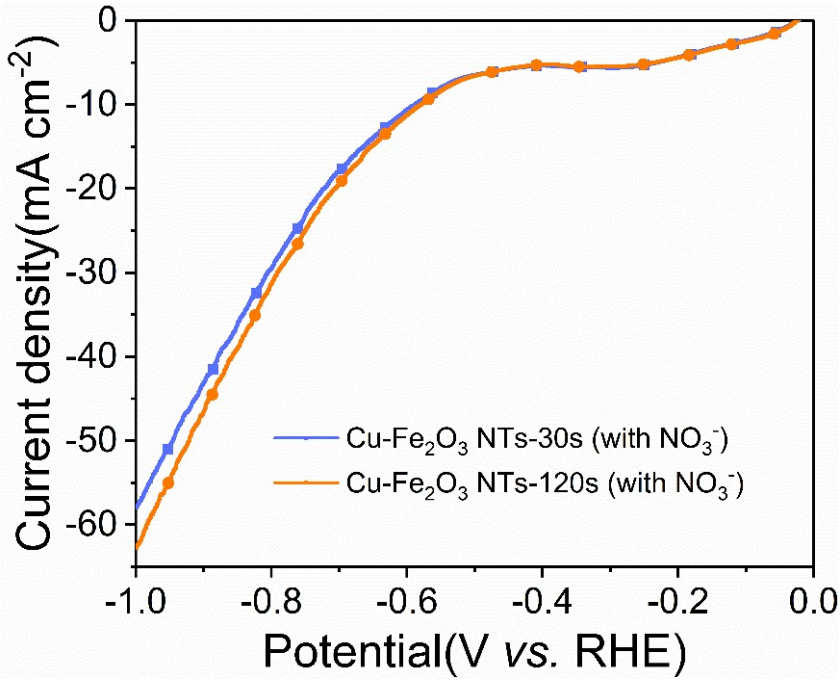

Fig. S11. LSV curves of Cu-Fe_2O_3-30 and Cu-Fe_2O_3-120 for nitrate reduction in 0.5 M Na_2SO_4 electrolyte containing 50 ppm NO_3^--N.

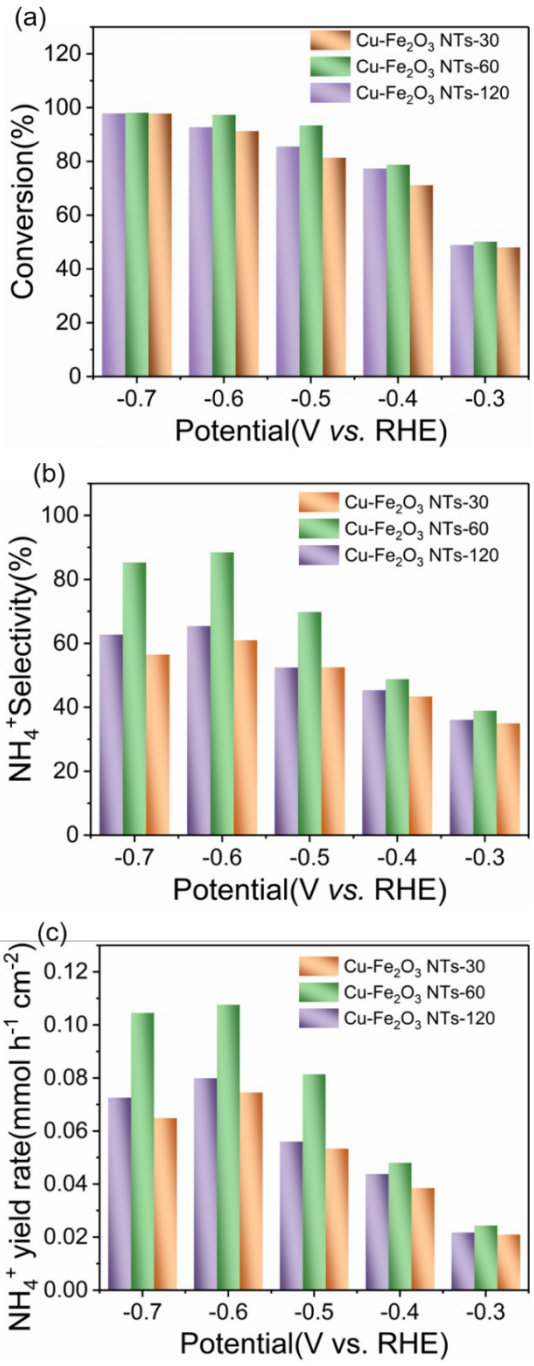

Fig. S12. (a) The conversion rate, (b) NH_4^+ selectivity and (c) NH_4^+ yield of Cu-Fe_2O_3 NTs-30, 60, 120 under different potentials.

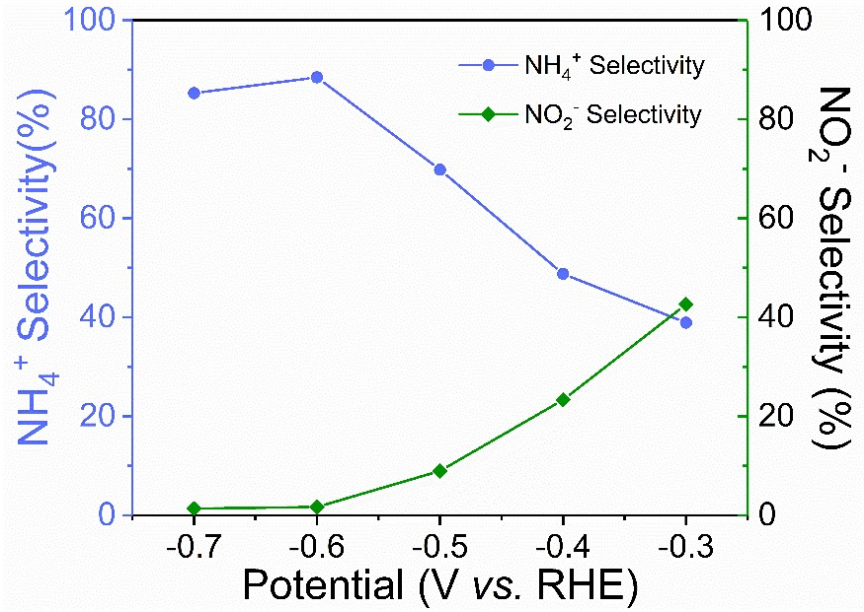

Fig. S13. The selectivity of nitrite and ammonium over Cu-Fe_2O_3-60 at given potential.

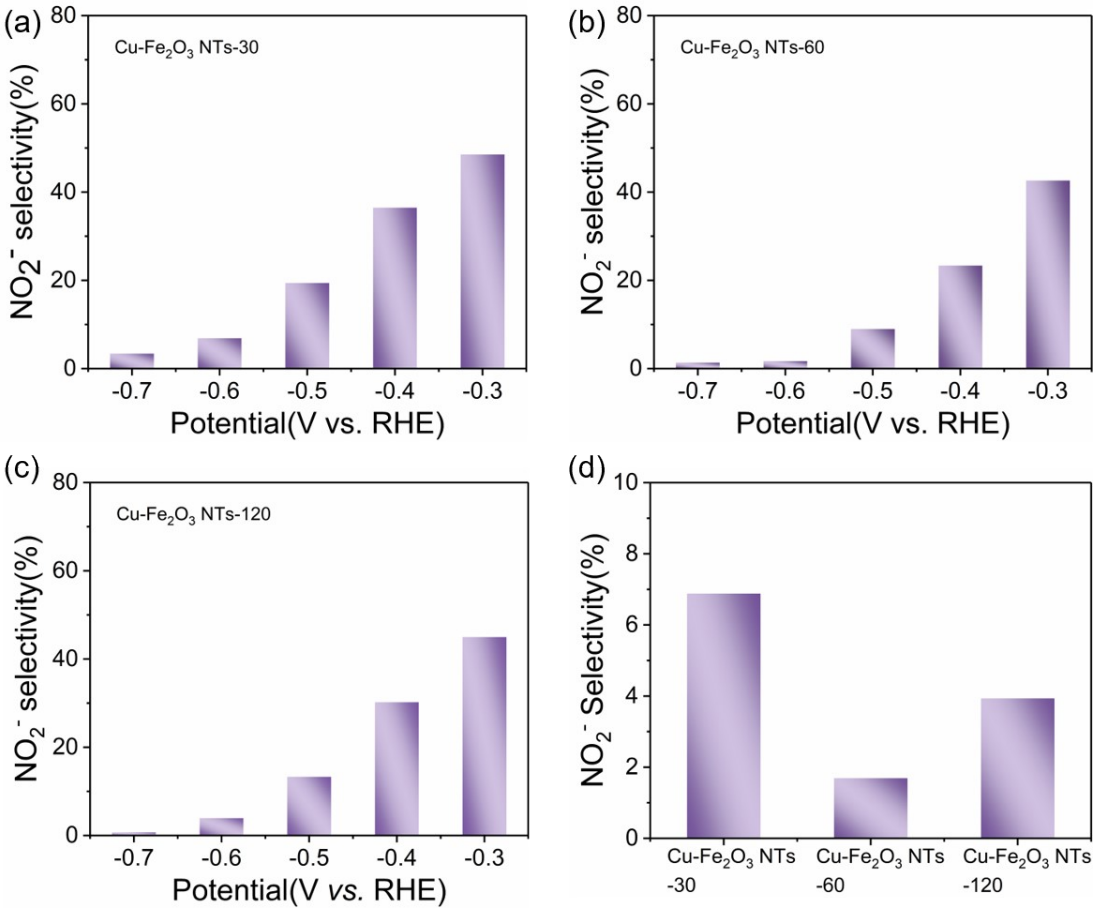

Fig. S14. The selectivity of nitrite of (a) Cu-Fe_2O_3 NTs-30, (b) Cu-Fe_2O_3 NTs-60, (c) Cu-Fe_2O_3 NTs-120 at given potentials. (d) The selectivity of nitrite of Cu-Fe_2O_3 NTs-30, Cu-Fe_2O_3 NTs-60, Cu-Fe_2O_3 NTs-120 at -0.6V *vs.* RHE.

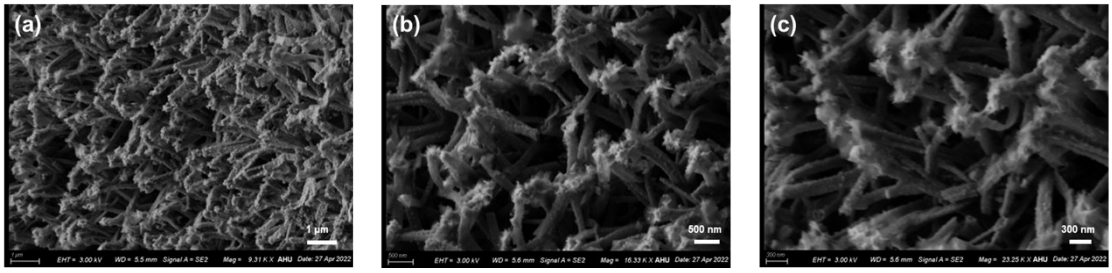

Fig. 15. The morphology of the Cu-Fe_2O_3-60 at different magnifications after testing.

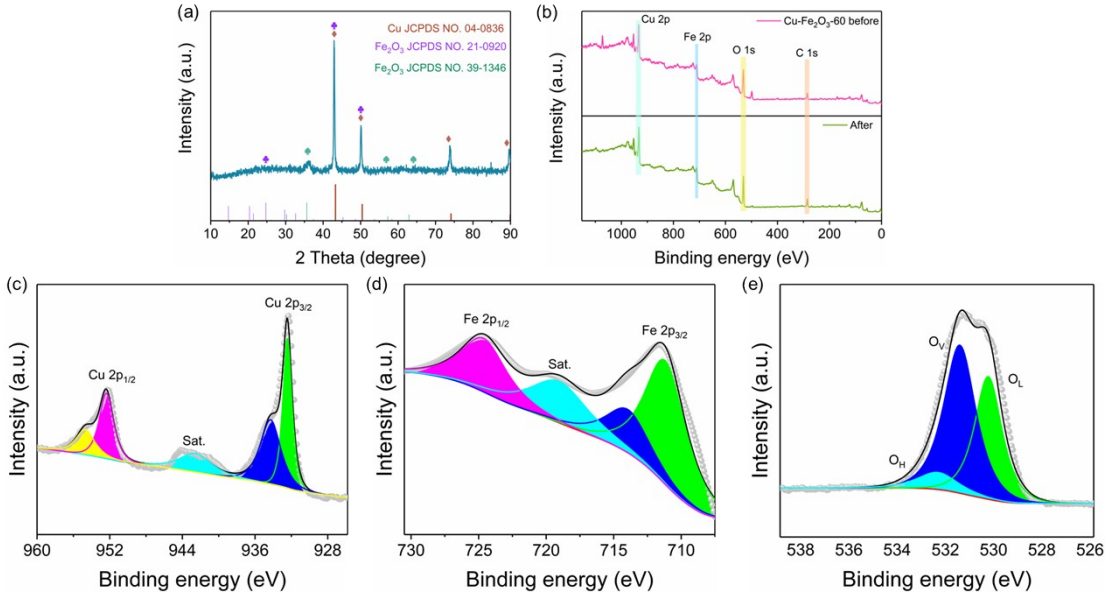

Fig. S16 (a) XRD pattern of Cu-Fe_2O_3-60 after repeated cyclic tests. (b) XPS all spectrum comparison of Cu-Fe_2O_3-60 before and after electrocatalysis test. High-resolution XPS spectra of (c) Cu 2p, (d) Fe 2p, (e) O 1s.

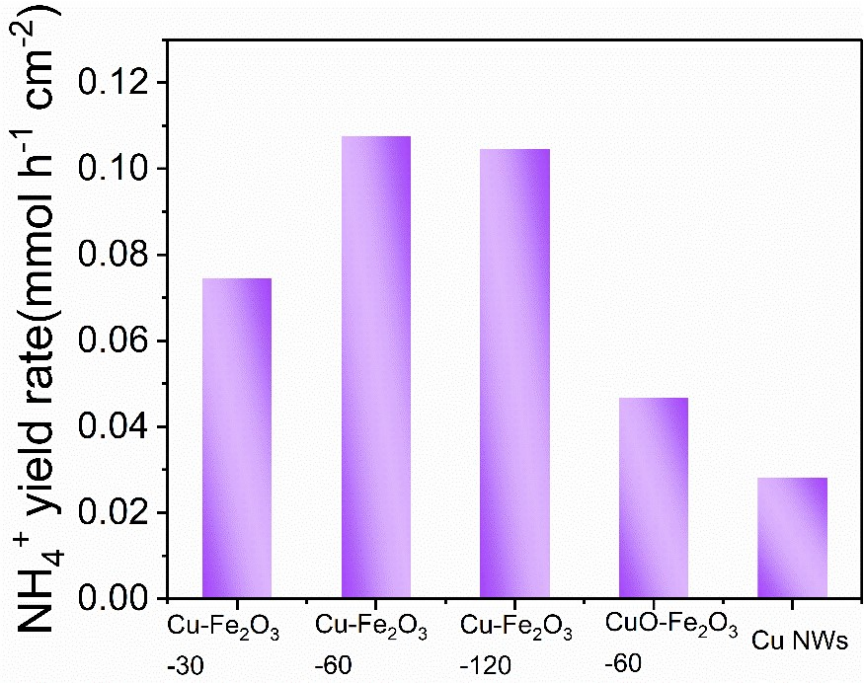

Fig. 17. The yield rates of ammonium over different samples at -0.6V *vs.* RHE.

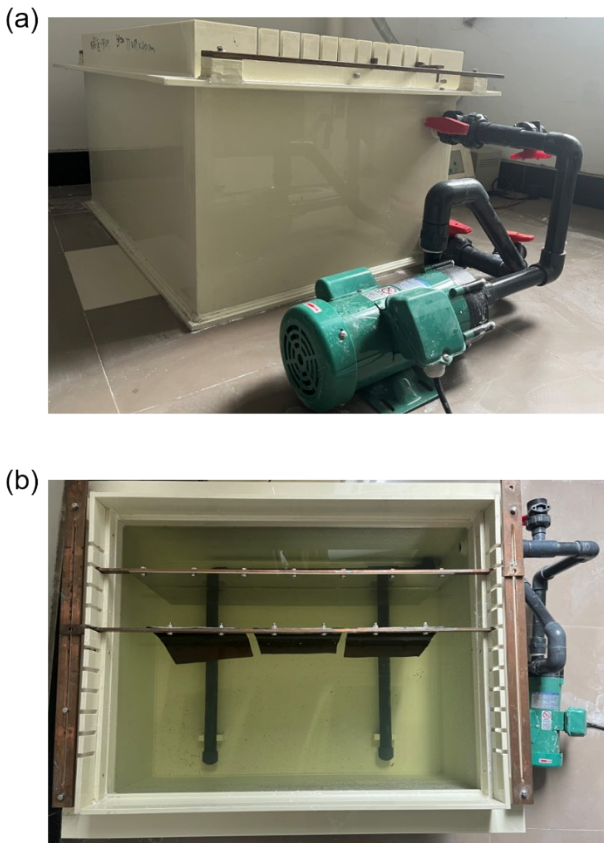

Fig. 18. The physical diagram of the reactor: (a) side view and (b) vertical view.

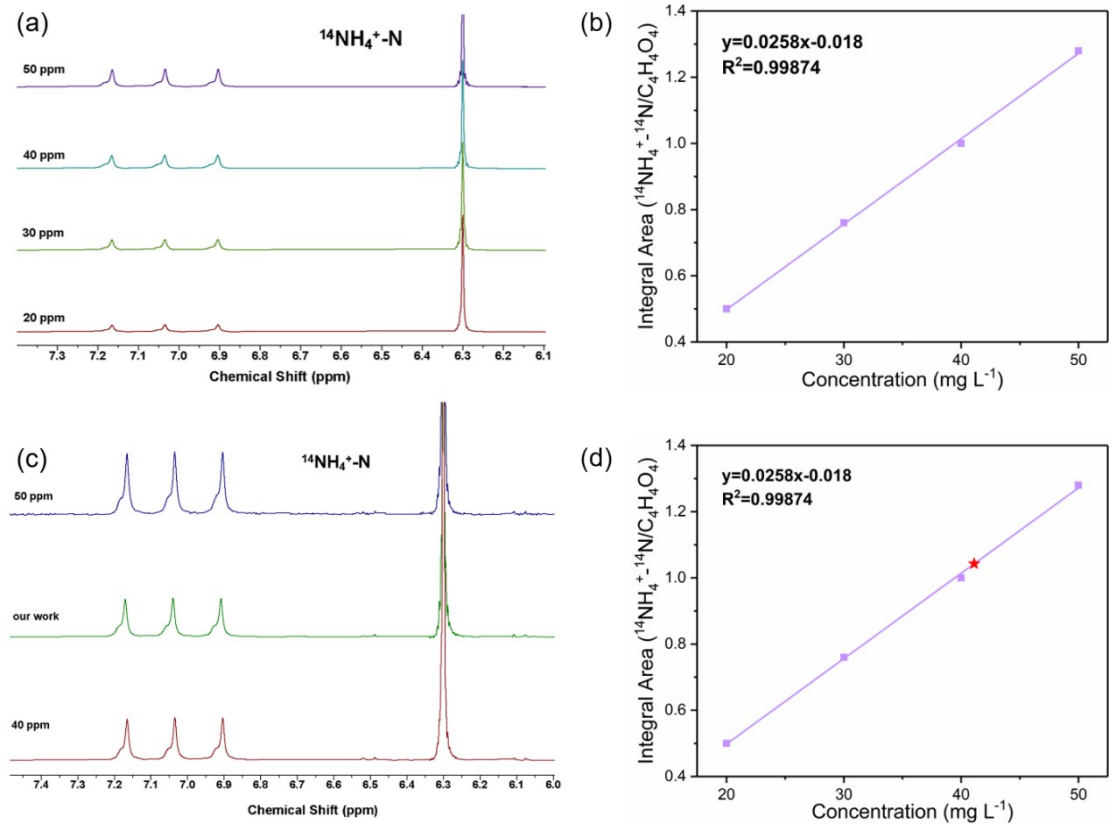

Fig. 19. (a) The ^1H NMR spectra (600 MHz) of $^{14}NH_4^+$ with different $^{14}NH_4^+$-^{14}N concentration. (b) Integral area ($^{14}NH_4^+$-^{14}N / $C_4H_4O_4$) against $^{14}NH_4^+$-^{14}N ion concentration ($^{14}NH_4^+$-^{14}N). (c) ^1H NMR spectra (600 MHz) of the electrolyte after $^{14}NO_3^-$ reduction over Cu-Fe_2O_3 NTs-60 at -0.6 V *vs.* RHE for 2 h. (d) The $^{14}NH_4^+$ ion concentration ($^{14}NH_4^+$-N) of the electrolyte that was quantified by ^1H NMR with maleic acid (300 ppm) as the reference.

The proton signal of maleic acid in Na_2SO_4 solution appears at δ = 6.29 ppm. The proton signals of $^{14}NH_4^+$ in Na_2SO_4 solution are observed at δ = 6.94 ppm, δ = 7.03 ppm and δ = 7.12 ppm.

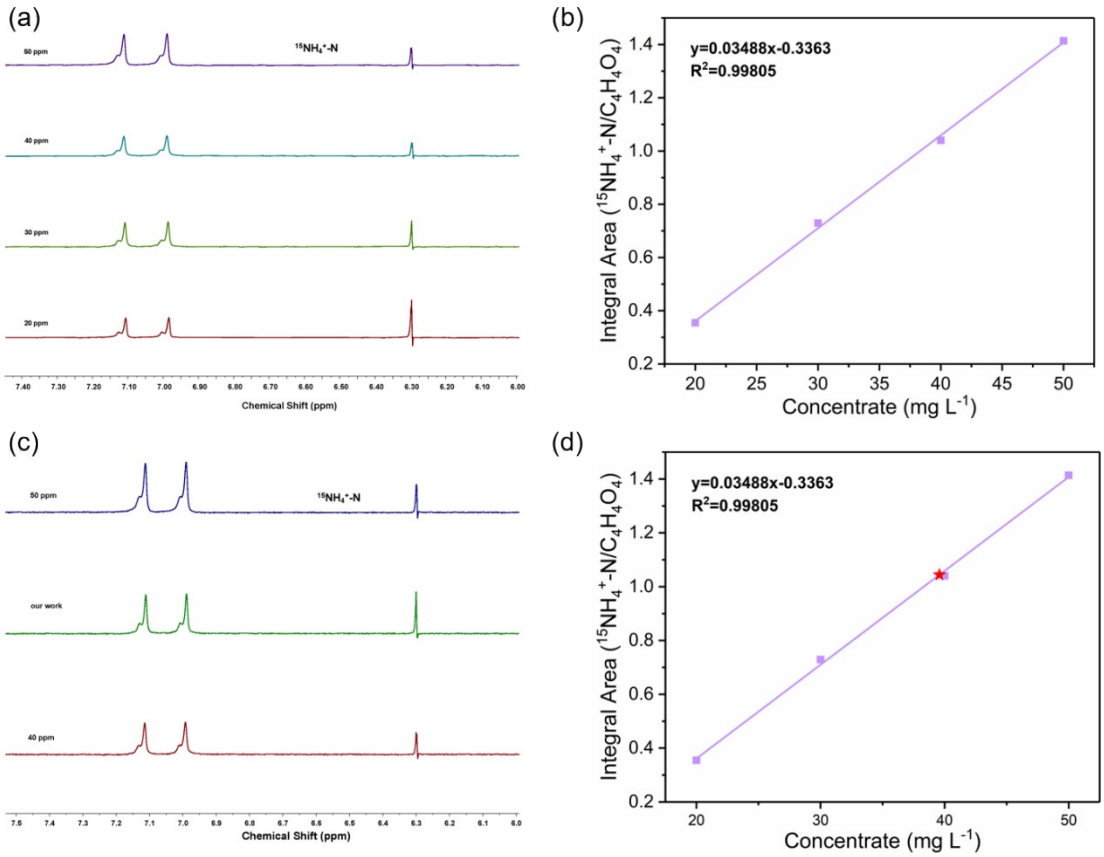

Fig. 20. (a) The ^{1}H NMR spectra (600 MHz) of $^{15}NH_4^+$ with different $^{15}NH_4^+$-^{15}N concentration. (b) Integral area ($^{15}NH_4^+$-^{15}N / $C_4H_4O_4$) against $^{15}NH_4^+$-^{15}N ion concentration ($^{15}NH_4^+$-^{15}N). (c) ^{1}H NMR spectra (600 MHz) of the electrolyte after $^{15}NO_3^-$ reduction over Cu-Fe_2O_3 NTs-60 at -0.6 V *vs.* RHE for 2 h. (d) The $^{15}NH_4^+$ ion concentration ($^{15}NH_4^+$-N) of the electrolyte that was quantified by ^{1}H NMR with maleic acid (300 ppm) as the reference.

The proton signal of maleic acid in Na_2SO_4 solution appears at δ = 6.29 ppm. The proton signals of $^{15}NH_4^+$ in Na_2SO_4 solution are observed at δ = 6.97 ppm and δ = 7.09 ppm.

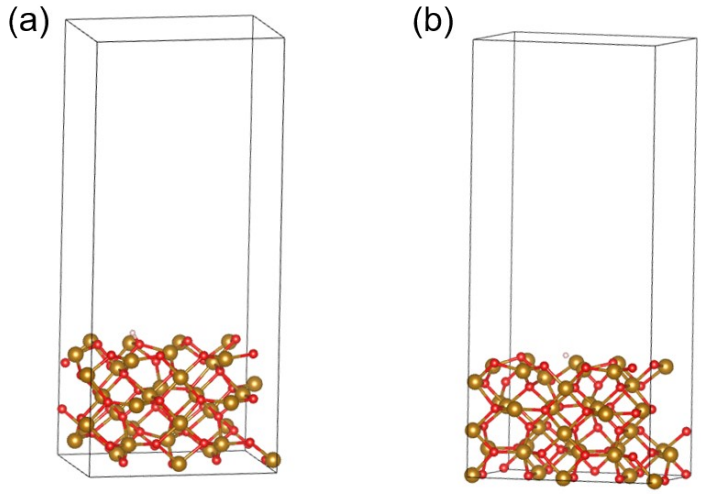

Fig. 21. Structural models of Cu-Fe_2O_3 NTs-60 (a) without and (b) with OVs.

Table S1. The cost of the materials per cm^2

Materials	Price	Amount	Total Cost
Copper Foam	120¥/(20cm×30cm)	1×3 cm^2	
NaOH	50¥/kg	0.7 g	0.4¥/cm^2
$(NH_4)_2S_2O_8$	40¥/kg	0.2 g	(Our work)
$Fe(NO_3)_3.9H_2O$	40¥/kg	0.01 g	
Ti foil	40.5¥(10cm×10cm)	1×3 cm^2	
Carbon Paper	430¥/(20cm×20cm)	1×3 cm^2	
NH_4F	480¥/kg	0.35 g	2.03¥/cm^2
ethylene glycol	38.5¥/500mL	70 mL	
5 wt% Nafion solution	17.5¥/mL	10 μL	
Nickel Foam	95¥/(20cm×30cm)	1×3 cm^2	1.51¥/cm^2
$Co(NO_3)_2$•$6H_2O$	1999¥/kg	2.037 g	
Nickel Foam	95¥/(20cm×30cm)	3×3 cm^2	
$C_6H_{11}FeNO_7$	238¥/kg	0.7 g	
C2H4N4	390¥/kg	5.6 g	0.5¥/cm^2
acetylene black	262¥/25g	10 mg	
PTFE, 5 wt%,	38¥/25g	200 mg	
Nickel Foam	95¥/(20cm×30cm)	2×2.5 cm^2	
$NiCl_2$	460¥/kg	0.02 g	
Phenolic resin	38¥/25 g	0.8 g	0.2¥/cm^2
Fe(NO3)3·9H2O	276¥/kg	0.2g	
citrate	74¥/kg	0.2854 g	
Nickel Foam	95¥/(20cm×30cm)	1×2 cm^2	
$NaH_2PO_2.H_2O$	990¥/kg	5 g	3.80¥/cm^2
Carbon Paper	430¥/(20cm×20cm)	1×2 cm^2	
5 wt% Nafion solution	17.5¥/mL	10 μL	

Table S2. Comparison of ammonium selectivity by electrocatalytic nitrate reduction.

Electrocatalysts	Electrolyte	Ammonia Selectivity	Ref.
Cu-Fe_2O_3-60 NTs	50ppm NO_3^--N +0.5M Na_2SO_4	88.47%	This work
TiO_{2-x} NTs	50ppm NO_3^--N +0.5M Na_2SO_4	87.1%	[15]
Co/CoO NSAs	200ppm NO_3^--N +0.5M Na_2SO_4	~71.48%	[16]
Fe@N-C	50ppm NO_3^--N +0.05M Na_2SO_4	73.43%	[17]
FeNi/g-mesoC/NF	50ppm NO_3^--N +0.05M Na_2SO_4	77.85%	[18]
Ni_2P@Ni	80ppm NO_3^--N +0.5M Na_2SO_4	89.1%	[19]

Table S3 The details on the nomenclature about the Cu-Fe_2O_3-x and contrast sample.

Sample name	immersion time(s)	Calcination conditions	electroreduction conditions
$Cu(OH)_2$-$Fe(OH)_3$-30	30		
$Cu(OH)_2$-$Fe(OH)_3$-60	60		
$Cu(OH)_2$-$Fe(OH)_3$-120	120		
CuO-Fe_2O_3-30	30	300°C	
CuO-Fe_2O_3-60	60	2h	
CuO-Fe_2O_3-120	120	air	
Cu-Fe_2O_3-30	30	300°C	20 mA cm^{-2}
Cu-Fe_2O_3-60	60	2h	15min
Cu-Fe_2O_3-120	120	air	

Table S4 C_{dl} and ECSA data of Cu-Fe_2O_3-30, Cu-Fe_2O_3-60 and Cu-Fe_2O_3-120 in electrocatalyst nitrate reduction.

Catalysts	C_{dl} (mF cm^{-2})	ECSA (cm^2)
Cu-Fe_2O_3-30	0.4585	27.51
Cu-Fe_2O_3-60	0.6755	40.53
Cu-Fe_2O_3-120	0.5651	33.91

Table S5. Comparison of the quantitative approach between colorimetric method and ^1H NMR for nitrate electroreduction at the optimal potential (-0.6 V *vs.* RHE).

Quantitative method	Nitrogen sources	Detected ion	Concentration (ppm)	Yield rate (mmol h^{-1} cm^{-2})
colorimetric method	$^{14}NO_3^-$-N	$^{14}NH_4^+$-N	43.055	0.1076
^{1}H NMR	$^{14}NO_3^-$-N	$^{14}NH_4^+$-N	41.085	0.1026
^{1}H NMR	$^{15}NO_3^-$-N	$^{15}NH_4^+$-N	39.601	0.0923

References

1. X. Cui, C. Tang and Q. Zhang, Adv. Energy Mater., 2018, 8, 1800369.
2. Z. Gong, W. Zhong, Z. He, Q. Liu, H. Chen, D. Zhou, N. Zhang, X. Kang and Y. Chen, Appl. Catal. B Environ., 2022, 305, 121021.
3. R. Mao, H. Zhu, K. Wang and X. Zhao, Appl. Catal. B Environ., 2021, 298, 120552.
4. D. Bao, Q. Zhang, F. Meng, H. Zhong, M. Shi, Y. Zhang, J. Yan, Q. Jiang and X. Zhang, Adv. Mater., 2017, 29, 1604799.
5. Y. Wang, Y. Yu, R. Jia, C. Zhang and B. Zhang, Natl. Sci. Rev., 2019, 6, 730-738.
6. Z. Geng, Y. Liu, X. Kong, P. Li, K. Li, Z. Liu, J. Du, M. Shu, R. Si and J. Zeng, Adv. Mater., 2018, 30, 1803498.
7. J. Hafner, J. Comput. Chem., 2008, 29, 2044-2078.
8. K. B. J.P. Perdew, M. Ernzerhof, Phys. Rev. Lett., 1996, 77, 3865-3868.
9. H. Xu, D. Cheng, D. Cao and X. Zeng, Nat. Catal., 2018, 1, 339-348.
10. J. R. J.K. Nørskov, A. Logadottir, L. Lindqvist, J. Phys. Chem. B, 2004, 108, 17886-17892.
11. T. Gu, W. Teng, N. Bai, Z. Chen, J. Fan, W. Zhang and D. Zhao, J. Mater. Chem. A, 2020, 8, 9545-9553.
12. J. Li, G. Zhan, J. Yang, F. Quan, C. Mao, Y. Liu, B. Wang, F. Lei, L. Li, A. W. M. Chan, L. Xu, Y. Shi, Y. Du, W. Hao, P. Wong, J. Wang, S. Dou, L. Zhang and J. Yu, J. Am. Chem. Soc., 2020, 142, 7036-7046.
13. J. Yang, P. Sebastian, M. Duca, T. Hoogenboom and M. T. M. Koper, Chem. Commun., 2014, 50, 2148-2151.
14. J. Zhu, Q. Xue, Y. Xue, Y. Ding, F. Li, P. Jin, P. Chen and Y. Chen, ACS Appl. Mater. Interfaces, 2020, 12, 14064-14070.
15. R. Jia, Y. Wang, C. Wang, Y. Ling, Y. Yu and B. Zhang, ACS Catal., 2020, 10, 3533-3540.
16. Y. Yu, C. Wang, Y. Yu, Y. Wang and B. Zhang, Sci. China Chem., 2020, 63, 1469-1476.
17. W. Duan, G. Li, Z. Lei, T. Zhu, Y. Xue, C. Wei and C. Feng, Water Res., 2019, 161, 126-135.
18. X. Chen, T. Zhang, M. Kan, D. Song, J. Jia, Y. Zhao and X. Qian, Environ. Sci. Technol., 2020, 54, 13344-13353.
19. Q. Yao, J. Chen, S. Xiao, Y. Zhang and X. Zhou, ACS Appl. Mater. Interfaces, 2021, 13, 30458-30467.